

When should we trust the annotation? Selective prediction for molecular structure retrieval from mass spectra

Mira Jürgens^{1*}, Gaetan De Waele², Morteza Rakhshaninejad¹, Willem Waegeman¹

^{1*}Department of Data Analysis and Mathematical Modeling, Ghent University, Coupure Links 653, Ghent, 9000, Belgium.

²Department of Computer Science, University of Antwerp, Middelheimlaan 1, Antwerp, 2020, Belgium.

*Corresponding author(s). E-mail(s): mira.juergens@ugent.be;
Contributing authors: gaetan.dewaele@uantwerpen.be;
morteza.rakhshaninejad@ugent.be; willem.waegeman@ugent.be;

Abstract

Machine learning methods for identifying molecular structures from tandem mass spectra (MS/MS) have advanced rapidly, yet current approaches still exhibit significant error rates. In high-stakes applications such as clinical metabolomics and environmental screening, incorrect annotations can have serious consequences, making it essential to determine when a prediction can be trusted. We introduce a selective prediction framework for molecular structure retrieval from MS/MS spectra, enabling models to abstain from predictions when uncertainty is too high. We formulate the problem within the risk-coverage tradeoff framework and comprehensively evaluate uncertainty quantification strategies at two levels of granularity: fingerprint-level uncertainty over predicted molecular fingerprint bits, and retrieval-level uncertainty over candidate rankings. We compare scoring functions including first-order confidence measures, aleatoric and epistemic uncertainty estimates from second-order distributions, as well as distance-based measures in the latent space. All experiments are conducted on the MassSpecGym benchmark. Our analysis reveals that while fingerprint-level uncertainty scores are poor proxies for retrieval success, computationally inexpensive first-order confidence measures and retrieval-level aleatoric uncertainty achieve strong risk-coverage tradeoffs across evaluation settings. We demonstrate that by applying distribution-free risk control via generalization bounds, practitioners can specify a tolerable error rate and obtain a subset of annotations satisfying that constraint with high probability.

Scientific contribution: This work provides the first systematic evaluation of selective prediction for molecular structure retrieval from mass spectra. We demonstrate that computationally inexpensive retrieval-level confidence measures outperform Bayesian epistemic uncertainty estimates for identifying reliable annotations, and that distribution-free risk control yields provable guarantees on annotation quality, transforming molecular identification into an uncertainty-aware decision process.

Keywords: metabolomics, molecular retrieval, uncertainty quantification, selective prediction, risk control

1 Introduction

Untargeted metabolomics generates vast numbers of tandem mass spectra (MS/MS), yet only approximately 10% of detected features can be annotated with molecular structures [1, 2], a deficit also known as *dark matter* of metabolomics [3, 4]. This difficulty stems from different sources, including a fundamental mismatch between the vast chemical space and the limited coverage of spectral reference libraries, the inherent complexity of molecular fragmentation, and the variability of spectra across instrument settings and ionization conditions. The correct identification of the molecular structure from a mass spectrum is hence considered a very challenging task, while being of fundamental importance with applications in drug discovery [5–7], environmental biochemistry [8, 9] and clinical diagnostics [10]. A growing body of literature uses machine learning methods to tackle this problem, where two main paradigms are formed by *molecular retrieval* [11–14] and *de novo structure elucidation* [15–18]. The retrieval paradigm, which is the focus of this work, predicts a molecular representation from the query spectrum and ranks candidate structures from a molecular database via a similarity function. The classical approach within this paradigm is molecular fingerprint prediction [11–13], where a model learns to map spectra to binary fingerprint vectors encoding the presence or absence of molecular substructures [19, 20]. More recently, joint embedding approaches avoid explicit fingerprint prediction and instead learn a shared latent space in which spectra and molecules can be compared directly via cosine similarity [14, 21].

The pace of progress in retrieval-based identification has been substantial. CSI:FingerID [11] trains an array of support vector machines, one per molecular property, using multiple kernel learning over fragmentation tree similarities to predict molecular fingerprints from MS/MS spectra. It was the first method to substantially outperform in silico fragmentation tools such as MetFrag [22] and CFM-ID [23], and became the core of the widely adopted SIRIUS framework [24]. MIST [13] subsequently introduced a transformer architecture that encodes MS/MS

peaks as chemical formula vectors rather than binned m/z values, thereby implicitly featurizing pairwise neutral losses between fragments. The introduction of the MassSpecGym benchmark [25], comprising 231,104 labeled spectra with structure-disjoint evaluation splits based on molecular similarity, provided a standardized basis for comparing retrieval methods. Joint embedding approaches, which embed molecules and spectra in a shared latent space and rank candidates by cosine similarity rather than by comparing explicit fingerprint reconstructions, have since demonstrated substantial improvements. JESTR [14] treats molecules and their spectra as two views of the same underlying object and trains molecular and spectral encoders jointly using contrastive multiview coding [26]. GMLR [27] initializes the molecular encoder from ChemFormer [28] and jointly finetunes it during contrastive training.

Despite this rapid progress, a significant error rate at the current state of the art remains consequential for downstream applications. In clinical metabolomics, incorrect identifications can delay or misdirect diagnosis of inborn errors of the metabolism [10]. In environmental nontarget screening, annotations directly inform regulatory decisions on chemical contamination [9]. These examples illustrate that predictive accuracy alone, without a mechanism to express the reliability of individual predictions, is insufficient for trustworthy metabolomics. To avoid making unreliable predictions, correct uncertainty quantification can help to build a trustworthy deployment of machine learning pipelines. *Selective prediction* [29–31] provides a powerful tool to reduce the error rate by abstaining from making a prediction when the uncertainty is too high. A selective classifier augments a prediction function with a selection function that determines, for each input, whether to predict or to abstain, thereby trading off *coverage*, i.e. the fraction of inputs on which the model commits, for lower *risk* on accepted predictions [31, 32]. The effectiveness of selective prediction depends on the scoring function that decides which predictions to trust. A natural source of such scores is predictive uncertainty, which can be decomposed into *aleatoric* uncertainty, arising from irreducible noise or ambiguity in the data, and *epistemic*

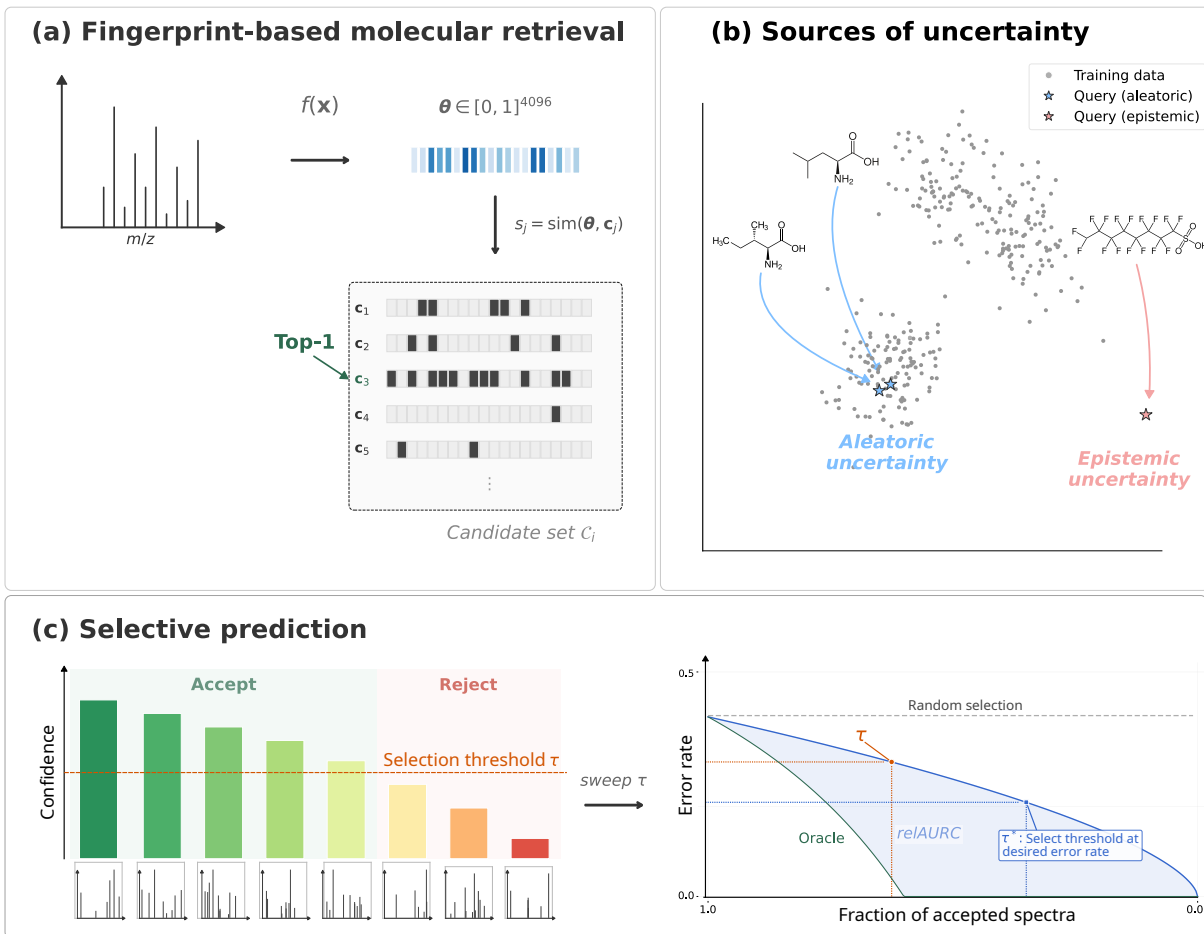


Fig. 1: Overview of the selective prediction framework for molecular structure retrieval from tandem mass spectra. **(a)** Fingerprint-based molecular retrieval. A tandem mass spectrum \mathbf{x} is mapped by a model f to a vector of bitwise probabilities $\boldsymbol{\theta} \in [0, 1]^{4096}$. Each candidate fingerprint \mathbf{c}_j in the instance-specific candidate set \mathcal{C}_i is scored by cosine similarity $s_j = \text{sim}(\boldsymbol{\theta}, \mathbf{c}_j)$, and candidates are ranked by descending score. **(b)** Sources of uncertainty in the learned representation space. Aleatoric uncertainty is due to inherent noise and ambiguity in the data, and can arise for structurally similar molecules. Epistemic uncertainty reflects a general lack of knowledge, and arises in regions of the representation space that are far from training data. **(c)** Selective prediction. Left: test spectra are sorted by confidence in descending order. A threshold τ partitions spectra into accepted and rejected predictions. Right: sweeping the threshold τ over its full range traces the risk-coverage curve, where different points on the curve correspond to different risk-coverage trade-offs.

uncertainty, reflecting the model’s lack of knowledge due to limited training data [33, 34]. In mass spectrometry, aleatoric uncertainty is inherent to the measurement process: structural isomers can produce nearly indistinguishable fragmentation patterns [35], and spectra of the same compound vary with collision energy, instrument type, and acquisition conditions. Epistemic uncertainty on

the other hand reflects limitations of the learned model, arising from finite training data, model misspecification, and distributional shift between train and test data. Until now, no empirical consensus exists for which of these uncertainty types is most informative for selective prediction. We therefore analyze both components separately

throughout this work.

In this work, we introduce a systematic selective prediction framework for molecular structure retrieval from MS/MS spectra (Figure 1). We formulate the retrieval problem within the risk-coverage tradeoff framework and conduct a comprehensive evaluation of uncertainty quantification strategies at two levels of granularity: *bitwise* uncertainty over predicted molecular fingerprint bits, and *retrieval-level* uncertainty over candidate rankings. We compare a broad range of selection criteria, including first-order confidence measures, epistemic uncertainty estimates from Bayesian approximations, and distance-based measures in the learned representation space. To provide finite-sample guarantees, we apply distribution-free risk control via the SGR algorithm [32], yielding provable bounds on the risk among accepted annotations. Our analysis reveals that while standard epistemic uncertainty estimates fail to improve selective prediction performance in this setting, computationally inexpensive first-order confidence measures based on retrieval provide effective selection functions. We demonstrate that selective prediction enables practitioners to specify a tolerable error rate and obtain a subset of annotations satisfying that constraint with high probability, transforming molecular identification into an uncertainty-aware decision process. Section 2 introduces the main framework, uncertainty estimation and evaluation methods, Section 3 presents the experimental evaluation and discussion, and Section 4 concludes with implications and limitations.

2 Methods

2.1 Fingerprint-based molecular retrieval

Let \mathcal{X} denote the input space of tandem mass spectra and let $\mathcal{Y} \subseteq \{0, 1\}^D$ denote the output space of molecular fingerprints, where $D \in \mathbb{N}$ is the fingerprint dimensionality. Each fingerprint is a binary vector encoding the presence or absence of predefined molecular substructures. We assume access to a dataset $\mathcal{D} = \{(\mathbf{x}_i, \mathbf{y}_i, \mathcal{C}_i)\}_{i=1}^N$ of N labeled instances, where $\mathbf{x}_i \in \mathcal{X}$ is a tandem mass spectrum, $\mathbf{y}_i \in \mathcal{Y}$ the molecular fingerprint of the true molecule, and $\mathcal{C}_i = \{\mathbf{c}_{i,1}, \dots, \mathbf{c}_{i,M_i}\} \subset \mathcal{Y}$ an

instance-specific candidate set of M_i molecular fingerprints retrieved from a chemical database. By construction, the true fingerprint satisfies $\mathbf{y}_i \in \mathcal{C}_i$. Molecular identification proceeds in two stages. First, a model $f : \mathcal{X} \rightarrow \Theta \subseteq [0, 1]^D$ predicts a vector of bitwise probabilities $\boldsymbol{\theta} = (\theta_1, \dots, \theta_D)^T$, where each component θ_d estimates the probability of the d -th substructure being present. Second, a similarity function $\text{sim} : [0, 1]^D \times \{0, 1\}^D \rightarrow \mathbb{R}$ is used to score each candidate $\mathbf{c} \in \mathcal{C}_i$ against the prediction. In this work we use the cosine similarity: For $j = 1, \dots, M_i$,

$$s_j(\mathbf{x}) = \text{sim}(\boldsymbol{\theta}, \mathbf{c}_j) = \frac{\boldsymbol{\theta}^\top \mathbf{c}_j}{\|\boldsymbol{\theta}\|_2 \|\mathbf{c}_j\|_2}. \quad (1)$$

Candidates are ranked by descending score, and the top- K set $\mathcal{S}_K(\mathbf{x}) \subset \mathcal{C}_i$ consists of the K highest-scoring candidates. Retrieval performance is measured by the *hit rate at K* ,

$$\text{Hit@}K(\mathbf{x}, \mathbf{y}) = \mathbb{I}[\mathbf{y} \in \mathcal{S}_K(\mathbf{x})], \quad (2)$$

where $\mathbb{I}[\cdot]$ denotes the indicator function, which equals one if the condition is satisfied and zero otherwise. This metric captures the practical utility of the retrieval pipeline, as it directly reflects the probability of the true molecule being among the top- K candidates. We evaluate $K \in \{1, 5, 20\}$ throughout this work. Two properties of this setting are particularly relevant for uncertainty quantification. First, the candidate set size M_i varies across instances, since it is determined by external database queries based on precursor mass or molecular formula. Second, the task exhibits a two-stage structure in which retrieval quality directly depends on the quality of the predicted fingerprint. Whether uncertainty at the bit level transfers to the retrieval level is analyzed in Section 3.

2.2 Selective prediction

In many applications, making no prediction is preferable to making an incorrect one [30, 31]. Selective prediction formalizes this idea by augmenting a predictor f with a *selection function* $g : \mathcal{X} \rightarrow \{0, 1\}$ that decides, for each input, whether to commit to the prediction or to abstain.

The resulting selective classifier (f, g) operates as

$$(f, g)(\mathbf{x}) = \begin{cases} f(\mathbf{x}), & \text{if } g(\mathbf{x}) = 1, \\ \text{abstain}, & \text{if } g(\mathbf{x}) = 0. \end{cases} \quad (3)$$

In practice, the selection function is defined via a *scoring function* $\kappa : \mathcal{X} \rightarrow \mathbb{R}$ that quantifies the model’s confidence in its prediction, together with a threshold $\tau \in \mathbb{R}$:

$$g_\tau(\mathbf{x}) = \mathbb{I}[\kappa(\mathbf{x}) \geq \tau]. \quad (4)$$

Instances for which the confidence falls below τ are rejected. Different choices of κ are compared in Section 2.3. The quality of a selective classifier is characterized by two quantities. The *coverage* measures the fraction of instances on which the model commits to a prediction,

$$\varphi(f, g) = \mathbb{E}[g(\mathbf{x})],$$

and the *selective risk* measures the expected loss restricted to accepted instances,

$$R(f, g) = \frac{\mathbb{E}[\ell(f(\mathbf{x}), \mathbf{y}) \cdot g(\mathbf{x})]}{\varphi(f, g)}, \quad (5)$$

where $\ell : \Theta \times \mathcal{Y} \rightarrow \mathbb{R}$ denotes a task-specific loss function. For the retrieval task, we define $\ell_K(f(\mathbf{x}), \mathbf{y}) = 1 - \text{Hit}@K(\mathbf{x}, \mathbf{y})$, so that $R(f, g)$ represents the miss rate among accepted predictions. The central trade-off in selective prediction is between risk and coverage: a more stringent threshold τ reduces the risk among selected instances but also lowers coverage. This trade-off is visualized through *risk-coverage curves*, which show the selective risk as a function of coverage for varying τ .

2.3 Scoring functions

The effectiveness of selective prediction depends critically on the scoring function $\kappa : \mathcal{X} \rightarrow \mathbb{R}$ that drives the selection function in Eqn. (4). A well-chosen κ assigns high values to inputs where the expected risk is low, enabling a favorable risk-coverage trade-off. Since the fingerprint-based retrieval pipeline operates in two stages, uncertainty can arise at different levels, and it is a priori unclear which characterization yields the most informative selection criterion. We therefore

investigate scoring functions from three complementary families, distinguished by the level on which uncertainty is measured: *fingerprint-level* scores derived from the predicted bit probabilities, *retrieval-level* scores operating on the induced candidate ranking, and *distance-based* scores that measure proximity to the training distribution in representation space. Within the first two families, we further distinguish between *first-order* scores that can be computed from a single model prediction, and *second-order* scores that require an approximate posterior distribution over model parameters. All κ are oriented so that higher values indicate greater confidence. Formal definitions of all scoring functions are given in Appendix A.

Candidate probabilities. Several scoring functions operate not on the raw similarity scores $s_j(\mathbf{x})$ but on a probability distribution over candidates. We obtain this by applying a temperature-scaled softmax,

$$p_j(\mathbf{x}) = \frac{\exp[s_j(\mathbf{x})/T]}{\sum_{k=1}^{M_i} \exp[s_k(\mathbf{x})/T]}, \quad (6)$$

for $j = 1, \dots, M_i$ and temperature parameter $T > 0$. The resulting distribution converts raw similarity scores into a categorical distribution over candidates, which serves as the basis for both the first-order and the uncertainty-decomposition-based scoring functions below.

First-order uncertainty scores. The simplest scoring functions require only a single predicted candidate distribution and no access to an ensemble or posterior approximation. The *confidence* $\kappa_{\text{conf}} = \max_j p_j(\mathbf{x})$ equals the probability assigned to the top-ranked candidate, following the maximum softmax probability baseline [36] widely used for misclassification detection. The *score gap* $\kappa_{\text{gap}} = s_{(1)}(\mathbf{x}) - s_{(2)}(\mathbf{x})$ measures the difference between the two highest pre-softmax similarity scores, indicating how separated the top candidate is from its nearest competitor. Both scores capture how peaked the candidate distribution is. Because they require no repeated inference, they are computationally inexpensive and applicable to any retrieval model.

Second-order uncertainty scores. A richer family of scoring functions decomposes predictive

Table 1: Overview of scoring functions κ investigated in this work. All scores are oriented so that higher values indicate greater confidence. “Order” indicates whether the score requires a single prediction (1st) or multiple posterior samples (2nd). Formal definitions are given in Appendix A.

Score	Level	Order	Description
κ_{conf}	Retrieval	1st	Max. candidate probability
κ_{gap}	Retrieval	1st	Difference between top-two similarity scores
$\kappa_{\text{bit}}^{\text{tot}}$	Fingerprint	2nd	Total predictive entropy (fingerprint)
$\kappa_{\text{bit}}^{\text{al}}$	Fingerprint	2nd	Aleatoric uncertainty (fingerprint)
$\kappa_{\text{bit}}^{\text{ep}}$	Fingerprint	2nd	Epistemic uncertainty (fingerprint)
$\kappa_{\text{ret}}^{\text{tot}}$	Retrieval	2nd	Total predictive entropy (candidate ranking)
$\kappa_{\text{ret}}^{\text{al}}$	Retrieval	2nd	Aleatoric uncertainty (candidate ranking)
$\kappa_{\text{ret}}^{\text{ep}}$	Retrieval	2nd	Epistemic uncertainty (candidate ranking)
κ_{rank}	Retrieval	2nd	Rank variance of top- K set across samples
κ_{knn}	Input	1st	Deep k -nearest-neighbor distance
κ_{mah}	Input	1st	Mahalanobis distance

uncertainty into aleatoric and epistemic components. This decomposition requires not a single prediction, but a distribution over predictions, obtained by placing a *second-order distribution* $q(\boldsymbol{\theta}|\mathbf{x})$ over the model’s predicted fingerprint probabilities [37]. In practice, this distribution is intractable and is approximated by drawing S samples, e.g. from independently trained ensemble members or stochastic forward passes. Given these samples, the information-theoretic decomposition [38] then decomposes the entropy of the averaged prediction (total uncertainty) into the mean entropy of individual sample predictions (aleatoric uncertainty) and their mutual information with the model parameters (epistemic uncertainty).

The decomposition can be applied at two levels. At the *fingerprint level*, each predicted bit probability θ_d is treated as a Bernoulli parameter, and the decomposition is applied independently to each of the D bits and then aggregated [39], yielding scores $\kappa_{\text{bit}}^{\text{tot}}$, $\kappa_{\text{bit}}^{\text{al}}$, and $\kappa_{\text{bit}}^{\text{ep}}$. At the *retrieval level*, the decomposition is instead applied to the candidate probability distributions induced by each posterior sample, yielding retrieval-level scores $\kappa_{\text{ret}}^{\text{tot}}$, $\kappa_{\text{ret}}^{\text{al}}$, and $\kappa_{\text{ret}}^{\text{ep}}$. These scores capture uncertainty about which candidate is correct rather than about individual fingerprint bits. Which level provides the more informative selection criterion is an empirical question addressed in Section 3.

As an additional second-order measure, we consider the *rank variance* κ_{rank} , which quantifies the stability of the top- K candidate set across posterior samples. For each input, the top- K candidates are identified under the mean prediction and re-ranked under every posterior sample, and the rank variance is the average variance of these ranks across samples. The motivation is structural: for $K = 1$, retrieval success reduces to identifying the top candidate, which confidence directly captures. For $K > 1$, it becomes a set-membership question, and the relevant uncertainty concerns the stability of the predicted set’s composition. Because it captures both closely spaced similarity scores and model disagreement, rank variance acts as an implicit measure of total predictive uncertainty at the ranking level [40].

Distance-based scores. The measures above quantify uncertainty via the model’s predictions. An orthogonal approach assesses whether the input itself lies in a region of the learned representation space that is well covered by the training data [41]. We consider the *deep k -nearest-neighbor distance* κ_{knn} [42], which measures the average Euclidean distance of the input’s penultimate-layer representation to its k nearest training neighbors, and the *Mahalanobis distance* κ_{mah} [43], which accounts for the covariance structure of the training representations. The rationale is that spectra far from the training distribution are more likely to be poorly predicted.

2.4 Risk control with statistical guarantees

The scoring functions of Section 2.3 rank inputs by confidence, but do not prescribe a specific threshold τ . In practice, a practitioner requires a concrete decision rule: Given a tolerable target risk rate r^* , which predictions should be accepted? Setting the threshold on a held-out set to match the target risk empirically does not account for finite-sample variability and can lead to violations of the target risk on new data [44]. We therefore adopt the *selection with guaranteed risk* (SGR) algorithm [32], a distribution-free procedure that chooses τ with provable guarantees on the selective risk. SGR finds a threshold τ^* such that

$$\mathbb{P}(R(f, g_{\tau^*}) > r^*) < \delta, \quad (7)$$

for user-specified target risk $r^* > 0$ and confidence level $0 < \delta < 1$. Using a held-out calibration set, the algorithm computes exact binomial tail bounds on the true selective risk at each candidate threshold and applies a union bound to preserve the overall confidence level δ . Among all thresholds satisfying the bound, SGR selects the one that maximizes coverage. Full algorithmic details are given in Appendix B. In our experiments, we randomly split the MassSpecGym test set into equally sized calibration and evaluation halves and set $\delta = 0.001$. The threshold τ^* is selected on the calibration half, while the reported coverages and empirical risks are measured on the evaluation half.

2.5 Evaluation

We evaluate the quality of different scoring functions for selective prediction twofold: by evaluating the area under the risk-coverage curve, and assessing the coverage of the risk-controlled selective classifier.

Risk-coverage curves. For a given scoring function κ which defines the selector g_τ , the *risk-coverage curve* is the parametric curve $\tau \mapsto (\varphi(f, g_\tau), R(f, g_\tau))$ obtained by varying the threshold τ over its full range. As τ increases, coverage decreases and, for a well-chosen κ , the selective risk decreases with it. The curve thus visualizes the trade-off between committing to more predictions and controlling the error rate

among them. Its quality is summarized by the *area under the risk-coverage curve*,

$$\text{AURC}(\kappa) = \int_0^1 R(\varphi) d\varphi, \quad (8)$$

where $R(\varphi)$ denotes the selective risk at coverage level φ , i.e. the value of $R(f, g_\tau)$ at the unique threshold τ satisfying $\varphi(f, g_\tau) = \varphi$. Lower values indicate a more favourable risk-coverage trade-off. In practice, the integral is approximated by sorting the test instances by descending value of the scoring function, computing the empirical selective risk at each coverage level, and applying the trapezoidal rule. The AURC of a scoring function is determined by two factors: the base error rate of the model and the ranking quality of the scoring function κ . A model with high overall error will have high AURC even if κ perfectly separates correct from incorrect predictions. Since this paper is concerned with the quality of the scoring function rather than the absolute performance of the underlying model, we need a metric that isolates the contribution of it from the base error rate. To this end, we compare against two reference values. The *oracle* $\text{AURC}_{\text{oracle}}$ is obtained by sorting instances by decreasing loss, thereby rejecting all incorrect predictions first. It represents the lowest achievable AURC for the given model and loss. The *random* baseline $\text{AURC}_{\text{random}}$ rejects instances in arbitrary order, yielding a constant risk equal to the overall error rate at every coverage level. We report the *relative AURC*,

$$\text{relAURC}(\kappa) = \frac{\text{AURC}(\kappa) - \text{AURC}_{\text{oracle}}}{\text{AURC}_{\text{random}} - \text{AURC}_{\text{oracle}}}, \quad (9)$$

which normalizes the excess over the oracle by the achievable range of improvement, giving $\text{relAURC} = 0$ for a perfect scoring function and $\text{relAURC} = 1$ for random rejection.

Coverage at target risk. For the risk-controlled setting, we report the *coverage at target risk*: given a target risk rate r^* and a confidence parameter $\delta > 0$, the SGR algorithm returns an optimal threshold τ^* used for deciding whether to accept or reject each prediction, guaranteeing that the true selective risk is bounded by r^* with probability at least $1 - \delta$. We report the empirical selective risk at this threshold on the held-out

evaluation data, and the corresponding coverage

$$\varphi(f, g_{\tau^*}) = \mathbb{E}[g_{\tau^*}(\mathbf{x})] = \mathbb{P}[\kappa(\mathbf{x}) \geq \tau^*],$$

whose empirical estimate is the fraction of instances for which the model commits to a prediction while satisfying the risk constraint. Higher coverage at the same target risk indicates a more informative scoring function. We evaluate this metric over a range of target risks τ^* , while also verifying that the empirical risk on the evaluation data respects the desired bound.

2.6 Experimental setup

Dataset. We use the MassSpecGym benchmark [25], which consists of 231 104 spectrum-molecule pairs covering 28 929 unique molecules. The data is split into training, validation and test sets by clustering on maximum common edge subgraph (MCES) distance [45], ensuring that no molecular structure appears in more than one split. This yields 194 119, 19 429, and 17 556 spectra covering 22 746, 3 185, and 2 998 molecules, respectively. Each molecule is represented by a 4096-dimensional Morgan fingerprint [19] computed with radius 2. For each spectrum, a candidate set \mathcal{C}_i is constructed by iteratively filtering molecules with matching molecular formula from three chemical databases of increasing size, until the cap of $|\mathcal{C}_i| \leq 256$ is reached [25]. The resulting candidate set sizes vary considerably across instances and directly affect task difficulty. This variation is analyzed further in Section 3.3 and Appendix C.1.

Model and training procedure. As base model we adopt the fingerprint predictor and training procedure of De Waele et al. [46].¹ The input spectrum is binned and mapped by a three-layer fully-connected neural network to fingerprint probabilities $\theta = \sigma(f(\mathbf{x})) \in [0, 1]^{4096}$. Architectural details are given in Appendix C.2. While more expressive architectures exist [13], the multi-layer perceptron (MLP) achieves competitive retrieval performance on MassSpecGym [46], and its standard feedforward structure permits

clean application of established posterior approximation methods without architectural modifications. The model is trained with a contrastive ranking loss that directly optimizes retrieval performance. For each training instance $(\mathbf{x}_i, \mathbf{y}_i, \mathcal{C}_i)$, the loss is the negative log-likelihood of the true candidate \mathbf{y}_i under the temperature-scaled softmax over the candidate set,

$$\ell_{\text{rank}}(\mathbf{x}_i, \mathbf{y}_i) = -\log \frac{\exp[s_{\mathbf{y}_i}(\mathbf{x}_i)/T]}{\sum_{j=1}^{M_i} \exp[s_j(\mathbf{x}_i)/T]}, \quad (10)$$

where $s_j(\mathbf{x})$ denotes the cosine similarity between the predicted probability vector as defined in Eqn. (1), and T is a temperature hyperparameter. We additionally train models with focal loss [47] on individual bits for the analysis of fingerprint-level uncertainty. In this setting, the predicted fingerprint retains its interpretation as a vector of per-bit probabilities rather than serving primarily as a retrieval embedding.

Uncertainty estimation. The fingerprint- and retrieval-level scoring functions described in Section 2.3 require a second-order distribution $q(\theta|\mathbf{x})$, which allows for the disentanglement of uncertainty estimates into aleatoric and epistemic components. Our primary second-order method, whose results are shown throughout the main text, is a Deep Ensemble [48] consisting of $S = 5$ copies of the full model, trained independently with different random initializations and data-loader shuffles. We additionally evaluate MC Dropout [49] using $S = 50$ stochastic forward passes, and the last-layer Laplace approximation [50] with $S = 50$ weight samples. For the distance-based scores κ_{knn} and κ_{mah} , we extract the 1024-dimensional penultimate-layer representations from a single ensemble member for all training and test spectra. Representations are ℓ_2 -normalized before distance computation. For κ_{knn} , we use $k = 100$ neighbors.

Evaluation losses. All primary analyses use the retrieval loss $\ell_K = 1 - \text{Hit}@K$ for $K \in \{1, 5, 20\}$. To test whether the alignment between scoring function and task loss extends bidirectionally, we additionally evaluate with fingerprint-level similarity losses $\ell_{\text{sim}} = 1 - \text{sim}(\hat{\mathbf{y}}, \mathbf{y})$ using Tanimoto, cosine, and Hamming loss as similarity measures. The results are given in Appendix D.1.

¹Our implementation is available at <https://github.com/mkjuergens/Selective-MSMS>.

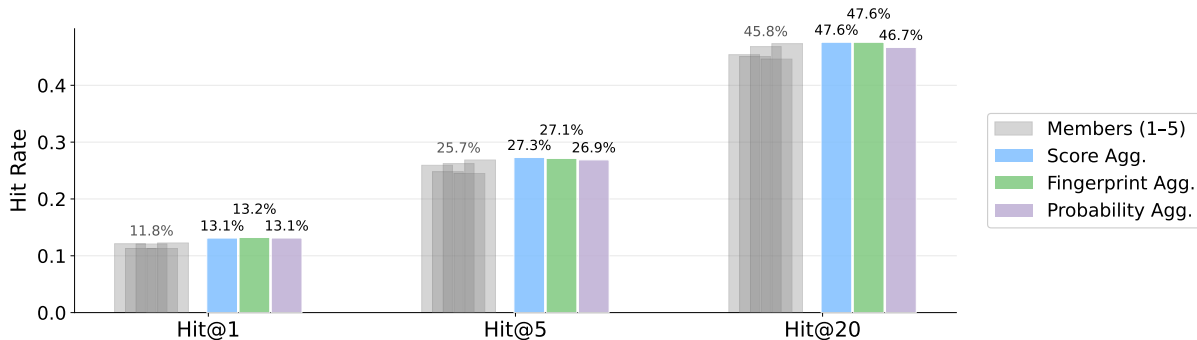


Fig. 2: Average Hit@ K rate for $K \in \{1, 5, 20\}$ for samples from the second-order distribution (grey) and their aggregate (blue, green, purple). Results are shown for a Deep Ensemble of $S = 5$ members and the experimental setup as described in Section 2.6, evaluated on the test set of MassSpecGym with candidates filtered by molecular formula. The aggregate is computed using the different aggregation strategies described in Section 2.6.

Prediction aggregation. Given S posterior samples $\theta_1, \dots, \theta_S$ from the second-order distribution $q(\theta|\mathbf{x})$, a single retrieval prediction must be produced. Aggregation on three different levels is possible:

1. Aggregation on the level of the fingerprints, where $\bar{\theta} = \frac{1}{S} \sum_{s=1}^S \theta_s$ is used for calculating similarity scores and ranking.
2. Aggregation on the level of similarity, where $\bar{s}_j = \frac{1}{S} \sum_{s=1}^S s_j(\mathbf{x}, \theta_s)$ is used for ranking.
3. Aggregation on the level of candidate probabilities, where $\bar{p}_j = \frac{1}{S} \sum_{s=1}^S p_j(\mathbf{x}, \theta_s)$ is used for ranking.

The three strategies of aggregation yield overall comparable retrieval performance. In the following, we adopt score-level aggregation when analyzing retrieval performance, and fingerprint-level aggregation when analyzing fingerprint similarity.

3 Results and discussion

All experiments are conducted on the MassSpecGym test set using the evaluation metrics and experimental setup as defined in Section 2.5. We first briefly analyze the baseline retrieval performance of the different uncertainty estimation methods and the effect of prediction aggregation. We then compare the effect of different scoring functions via a risk-coverage analysis, and subsequently examine how the candidate set size influences selective prediction quality. Finally, we

assess the coverage attainable under risk guarantees for different target risks.

3.1 Baseline retrieval performance

Table 2 reports the retrieval performance of the aggregate of the three different uncertainty estimation methods as well as a single-model baseline on the MassSpecGym test set. For both training objectives, aggregating over multiple posterior samples consistently improves hit rates relative to the single model, with the Deep Ensemble leading to the biggest improvement. Across the three second-order methods, the aggregate of the Deep Ensemble trained with ranking loss leads to the highest hit rates. Figure 2 illustrates the per-member variability and the effect of aggregation. Individual members exhibit considerable variance in hit rate, and their predictions disagree on a substantial fraction of test instances.

3.2 Risk-coverage curves

To evaluate how effectively each scoring function reduces the selective risk, we use the metrics described in Section 2.5, with the retrieval loss $\ell_K = 1 - \text{Hit}@K$, for $K \in \{1, 5, 20\}$. Figure 3 shows the obtained risk-coverage curves and the corresponding AURC values for the Deep Ensemble model trained with ranking loss. Table 3 reports the corresponding relative AURC values across all three second-order methods. Interestingly, the best scoring function depends on the size of the selected set \mathcal{S}_K for which the hit rate

Table 2: Retrieval performance on the MassSpecGym test set for the MLP architecture discussed in Section 2.6 trained with ranking loss, and different second-order uncertainty estimation methods. Hit@ K (%) denotes the fraction of test spectra for which the correct molecule appears among the top- K retrieved candidates. S denotes the number of posterior samples (ensemble members or stochastic forward passes). Aggregate: prediction obtained by averaging the S predicted scores before ranking. Avg. sample: mean Hit@ K across the S individual predictions.

Training loss	Method	Aggregate			Avg. sample		
		Hit@1	Hit@5	Hit@20	Hit@1	Hit@5	Hit@20
Focal	Single model	10.70	22.66	40.65	—	—	—
	Deep Ensemble ($S=5$)	11.43	23.80	42.36	10.71	22.67	40.70
	MC Dropout ($S=50$)	11.13	22.78	40.75	10.33	22.10	40.15
	Laplace ($S=50$)	11.22	22.62	41.39	11.01	22.65	41.38
Ranking	Single model	11.85	25.66	45.84	—	—	—
	Deep Ensemble ($S=5$)	13.12	27.29	47.57	11.83	25.66	45.83
	MC Dropout ($S=50$)	11.83	25.91	45.56	11.49	25.32	44.67
	Laplace ($S=50$)	12.21	26.83	47.25	12.11	26.35	46.81

is evaluated. For $K = 1$, the score gap achieves the lowest relative AURC for the Deep Ensemble. This is intuitive: the hit rate at $K = 1$ directly corresponds to the zero-one loss on the top candidate, and the score gap measures precisely how well separated that candidate is from its nearest competitor in pre-softmax similarity space. Confidence and aleatoric uncertainty, which both measure how peaked the candidate distribution is, perform comparably to each other but are less effective than the score gap. An analysis of the correlation between the different scores can be found in Appendix D. As K increases, the rank variance becomes more meaningful. The reason is that the hit rate for $K > 1$ is no longer a question about the candidate with highest probability alone, but about set membership, i.e. whether the correct candidate falls within the top- K set. The candidate set size shows a similar trend and correlates strongly with rank variance (see Appendix D.2), however, the rank variance remains the stronger criterion. Across all values of K , the retrieval-level epistemic uncertainty score is consistently inferior to all other retrieval-level scores. This finding is consistent with the theoretical analysis of Hofman et al. [51], who prove that for selective prediction with a given task loss, the optimal rejection criterion is the total predictive uncertainty instantiated with it, and hence not its epistemic component alone. Intuitively, for deciding whether to trust a

particular prediction, what matters is the overall expected loss of that prediction, which conflates both aleatoric difficulty and epistemic ignorance. The epistemic component alone discards the aleatoric contribution and therefore provides a strictly less informative ranking.

All bitwise uncertainty scores achieve relative AURC values at or above 0.9, making them barely distinguishable from random rejection. This is expected: retrieval success depends not on the absolute quality of the predicted fingerprint but on the *relative* similarity between the predicted fingerprint and the correct candidate versus its competitors. A spectrum whose fingerprint is confidently predicted may still fail at retrieval if multiple candidates share similar substructures, while a noisier prediction can succeed when the correct candidate is structurally distinct from all alternatives. The fingerprint-level uncertainty thus quantifies a necessary but insufficient condition for retrieval success, making it a poor proxy for the actual task loss. Conversely, when the evaluation loss is a fingerprint-level similarity, bitwise total uncertainty becomes the strongest scoring function. See Appendix D.1 for the corresponding risk-coverage analysis with similarity losses. This confirms that the alignment between the scoring function and the level at which the task loss operates is the primary determinant of selective prediction quality. The distance-based scores κ_{knn}

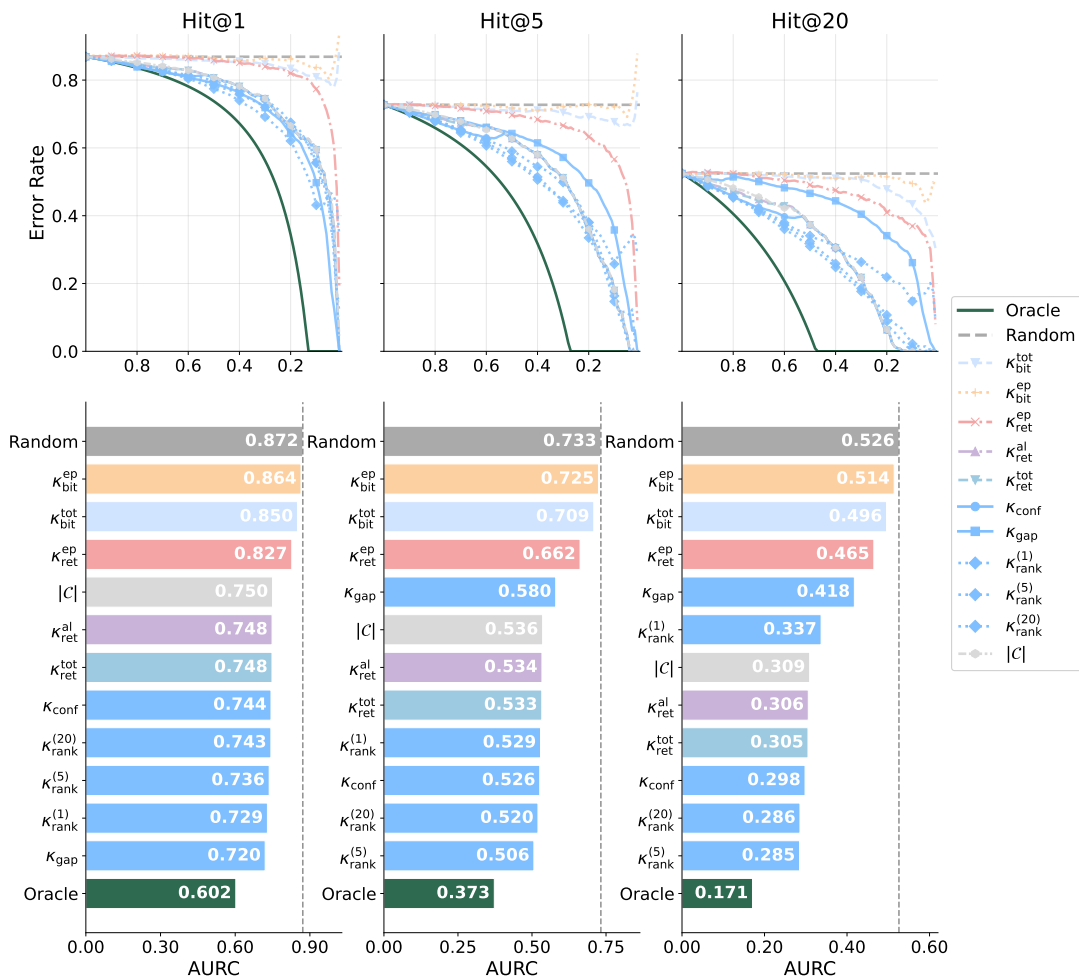


Fig. 3: Risk-coverage analysis for different scoring functions κ based on different uncertainty estimates as described in Section 2.3. The selective risk is calculated using $\ell_K = 1 - \text{Hit}@K$ for $K \in \{1, 5, 20\}$. Results are shown for a Deep Ensemble of $S = 5$ members and the experimental setup as described in Section 2.6, evaluated on the test set of MassSpecGym with candidates filtered by molecular formula. Colors encode the uncertainty component: blue tones indicate total uncertainty, purple indicates aleatoric uncertainty, and red tones indicate epistemic uncertainty. Darker shades correspond to retrieval-level scores, lighter shades to fingerprint-level scores. (a) Risk-coverage curves. (b) AURC values.

and κ_{mah} exhibit the same near-random behavior (Table 3). These measures assess whether a test spectrum lies in a well-covered region of the learned representation space. However, this space is shaped entirely by the training objective and has no reason to organize spectra by retrieval difficulty [52]. The relative ordering of scoring functions is preserved across all three second-order uncertainty estimation methods. The absolute values differ across methods, reflecting differences in the

quality of the posterior approximation, but the qualitative conclusions are unchanged.

3.3 Candidate set size analysis

A distinguishing feature of the retrieval setting is that the task difficulty varies across instances through the candidate set size $|C|$, which ranges from one to the benchmark cap of 256 and is determined by external database queries. Figure 4(a) confirms the expected effect: hit rates decrease

Table 3: Selective prediction quality for different scoring functions, evaluated by relAURC (Eqn. 9). Lower is better. Results are shown for different second-order uncertainty estimation methods and the experimental setup described in Section 2.6, evaluated on the test set of MassSpecGym with candidates filtered by molecular formula. The selective risk is evaluated using hit rate, $\ell_K = 1 - \text{Hit}@K$, $K = 1, 5, 20$. relAURC = 0 corresponds to perfect (oracle) rejection, relAURC = 1 corresponds to random rejection.

κ	Deep Ensemble			MC Dropout			Laplace		
	ℓ_1	ℓ_5	ℓ_{20}	ℓ_1	ℓ_5	ℓ_{20}	ℓ_1	ℓ_5	ℓ_{20}
<i>Retrieval-level</i>									
κ_{conf} confidence	0.525	0.426	0.359	0.402	0.440	0.524	0.515	0.410	0.350
κ_{gap} score gap	0.439	0.576	0.696	0.469	0.593	0.705	0.465	0.627	0.733
$\kappa_{\text{ret}}^{\text{al}}$ aleatoric	0.541	0.447	0.381	0.376	0.367	0.405	0.528	0.426	0.364
$\kappa_{\text{ret}}^{\text{ep}}$ epistemic	0.836	0.805	0.829	0.468	0.508	0.514	0.886	0.904	0.901
κ_{rank} $K=1$	0.472	0.434	0.468	0.505	0.480	0.520	0.713	0.686	0.729
κ_{rank} $K=5$	0.498	0.372	0.321	0.497	0.381	0.332	0.533	0.418	0.428
κ_{rank} $K=20$	0.524	0.410	0.324	0.499	0.395	0.327	0.528	0.404	0.345
<i>Fingerprint-level</i>									
$\kappa_{\text{bit}}^{\text{tot}}$ total	0.920	0.934	0.915	0.900	0.906	0.900	0.945	0.940	0.928
$\kappa_{\text{bit}}^{\text{al}}$ aleatoric	0.957	0.945	0.915	0.946	0.946	0.925	0.965	0.961	0.937
$\kappa_{\text{bit}}^{\text{ep}}$ epistemic	0.973	0.978	0.968	0.972	0.947	0.934	0.980	0.993	0.971
<i>Input-level[†]</i>									
κ_{knn} k -NN distance	0.985	0.915	0.929	—	—	—	—	—	—
κ_{mah} Mahalanobis	0.977	0.928	0.893	—	—	—	—	—	—
<i>Other</i>									
$ \mathcal{C} $ num. candidates	0.548	0.453	0.390	0.511	0.420	0.369	0.531	0.432	0.373

[†]Distance-based scores depend only on the encoder representation, not the posterior approximation method. Values shown are for one Deep Ensemble member. See Appendix A.3.

almost monotonically with $|\mathcal{C}|$. To analyze the effect of candidate set size as a selection criterion, we stratify the test set into instances with varying number of candidates ($|\mathcal{C}| < 256$) and instances with maximum number of candidates ($|\mathcal{C}| = 256$). When candidate sets vary in size, the gap between oracle and random rejection is wide and the scoring functions recover a substantial fraction of the achievable improvement, as can be seen in Figure 4 (b). At the cap, this gap shrinks and all scoring functions compress toward the random baseline, reflecting the increased difficulty, see Figure 4 (c). The candidate set size itself, which is an effective rejection criterion when it varies, becomes uninformative once it is constant. This illustration shows the role of the rank variance κ_{rank} as a selection criterion. Because it correlates strongly with the number of candidates, its good performance in the overall analysis is partly explained by this sensitivity: larger sets produce more candidates with similar scores near the decision boundary, thereby

inflating the rank variance. However, the stratified view reveals that rank variance is not merely a proxy for the number of candidates: for the subset of instances with maximum number of candidates, rank variance still achieves AURC values comparable to confidence and clearly below the random baseline. This suggests that it captures both the task difficulty given by the number of candidates, and ranking instability in general.

3.4 Coverage under risk control

The previous sections evaluated scoring functions by their ability to *rank* predictions, asking which ones correlate best with retrieval success. We now turn to the question that matters most in practice: given a tolerable error rate, how many spectra can be annotated with a formal correctness guarantee? Figure 5 (top row) shows the coverage obtained by applying the SGR algorithm across a range of

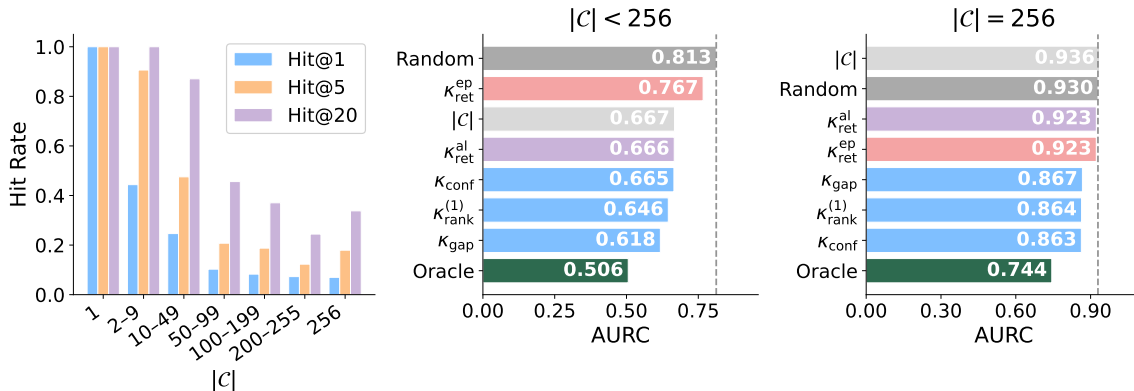


Fig. 4: Effect of the candidate set size on the retrieval performance and selective prediction quality. Results are shown for a Deep Ensemble of $S = 5$ members and the experimental setup as described in Section 2.6, evaluated on the test set of MassSpecGym with candidates filtered by molecular formula. **Left:** Average hit rate on subsets with binned candidate set size $|C|$. **Middle, Right:** AURC values for $\ell_1 = 1 - \text{Hit@1}$ and different scoring functions, on subsets of data with $|C| < 256$ vs. $|C| = 256$.

target risk levels. We see that the practical utility of risk-controlled selection depends strongly on the task difficulty and the chosen risk level. For controlling the hit rate at $K = 20$, where the base error rate is moderate, SGR retains up to 87% of test spectra at a target risk of $r^* = 0.5$. For $K = 1$, however, the base error rate is high and the algorithm can only guarantee risk control on a small subset of the data. This is not a limitation of the scoring functions but of the task itself: when the majority of predictions are incorrect, any procedure with valid risk guarantees must reject most instances. In practice, this means that exact-match identification requires either stronger base models or an acceptance of lower coverage, whereas candidate-list settings already offer a practical operating regime for automated annotation. Among scoring functions, confidence and score gap together with rank variance achieve the highest coverage across all settings, consistent with the results in Section 3.2. Figure 5 (bottom row) validates the statistical guarantee, showing that the empirical risk on the held-out evaluation half closely tracks the target without systematic violation, confirming that the bound transfers beyond the calibration data.

4 Conclusion

We introduced a selective prediction framework for molecular structure retrieval from tandem

mass spectra and conducted a systematic evaluation of uncertainty quantification strategies on the MassSpecGym benchmark. By formulating retrieval as a selective classification problem with task-specific losses, we evaluated scoring functions from three complementary families, acting on the level of the molecular fingerprints, the retrieval candidates, and the model’s internal representation space. We assessed their performance in terms of risk-coverage trade-offs, and showcased how generalization bounds can be used to obtain subsets of predictions with global risk guarantees. Our analysis reveals that the effectiveness of a scoring function depends critically on the level at which it operates relative to the task loss. Overall, retrieval-level scoring functions provide the most effective selection criteria when the task loss is hit rate. The optimal criterion shifts with the retrieval granularity: for exact-match retrieval, the first-order confidence score performs comparably to the second-order aleatoric uncertainty estimate, while for relaxed retrieval, the second-order rank variance becomes the strongest criterion. What unites all effective scoring functions is that they operate at the retrieval level and reflect total predictive uncertainty rather than isolating the epistemic component alone. This loss dependence extends to the granularity of uncertainty estimation itself. Fingerprint-level uncertainty, which quantifies how well the model predicts individual molecular substructures, is naturally aligned with

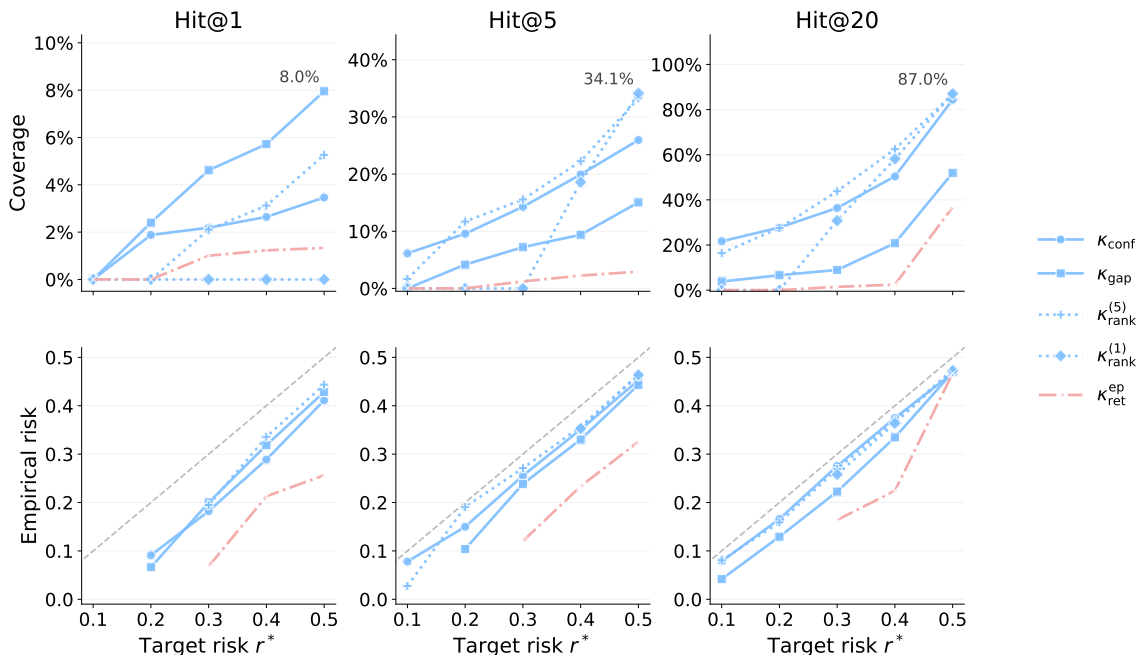


Fig. 5: Risk-controlled annotation with the SGR algorithm with $\delta = 0.001$ and different target risks r^* . Results are shown for a Deep Ensemble of $S = 5$ members and the experimental setup as described in Section 2.6, evaluated on the test set of MassSpecGym with candidates filtered by molecular formula. The scoring functions used for selection are the ones with the strongest risk-coverage trade-offs from Section 3.2. The threshold τ^* is calibrated on one half of the test set, coverage and empirical risk are evaluated on the held-out other half. **Top:** coverage attained at each target risk level r^* for $K \in \{1, 5, 20\}$. Note the independent vertical scales. **Bottom:** empirical risk versus target risk. All points lie below the diagonal, confirming the finite-sample guarantee.

fingerprint reconstruction quality but proves a poor proxy for retrieval success, where what matters is the *relative* similarity between the predicted fingerprint and the correct candidate versus its competitors. A spectrum whose fingerprint is confidently predicted may still fail at retrieval when structurally similar candidates are present, and conversely, a noisier prediction can succeed when the correct candidate is well separated. Epistemic uncertainty, whether at the fingerprint or retrieval level, is consistently outperformed by its total or aleatoric counterpart, consistent with the theoretical result of Hofman et al. [51] that for selective prediction the optimal scoring function is the total predictive uncertainty instantiated with the task loss. Distance-based scores, intended to flag inputs far from the training distribution, likewise provide limited selective prediction value, suggesting that the notion of epistemic uncertainty they capture is

not the primary driver of retrieval failure. Applying the SGR algorithm, we demonstrated that practitioners can specify a tolerable risk rate and obtain subsets of annotations satisfying the constraint with high probability, with the empirical risk on held-out data remaining below the target across all evaluated settings. Several limitations suggest directions for future research. Our experiments use a single base architecture, as the focus of this work is on analyzing uncertainty estimates for selective prediction rather than maximizing retrieval performance. Evaluating the framework on more expressive models, including transformer-based fingerprint predictors, would test whether the relative ordering of scoring functions transfers across accuracy regimes. On the methodological side, uncertainty estimation methods that account for the extreme sparsity of molecular fingerprints, or that assess epistemic uncertainty directly in the input space of spectra rather than in learned

representations shaped by the training objective, may yield more informative estimates than the standard decompositions evaluated here. Beyond selective prediction, false discovery rate control via the conformalized Benjamini–Hochberg procedure [53] offers a more stringent error criterion, providing bounds on the proportion of incorrect annotations rather than the average selective risk. Conformal prediction methods that output calibrated prediction sets [54] provide an alternative paradigm entirely.

Acknowledgements. M.J. and W.W. received funding from the Flemish Government under the “Onderzoeksprogramma Artificiële Intelligentie (AI) Vlaanderen” programme.

References

- [1] Böcker, S., Dührkop, K.: Fragmentation trees reloaded. *Journal of cheminformatics* **8**(1), 5 (2016)
- [2] Hähnke, V.D., Kim, S., Bolton, E.E.: Pubchem chemical structure standardization. *Journal of cheminformatics* **10**(1), 36 (2018)
- [3] Silva, R.R., Dorrestein, P.C., Quinn, R.A.: Illuminating the dark matter in metabolomics. *Proceedings of the National Academy of Sciences* **112**(41), 12549–12550 (2015)
- [4] Bittremieux, W., Wang, M., Dorrestein, P.C.: The critical role that spectral libraries play in capturing the metabolomics community knowledge. *Metabolomics* **18**(12), 94 (2022)
- [5] Aebersold, R., Mann, M.: Mass spectrometry-based proteomics. *Nature* **422**(6928), 198–207 (2003)
- [6] Meissner, F., Geddes-McAlister, J., Mann, M., Bantscheff, M.: The emerging role of mass spectrometry-based proteomics in drug discovery. *Nature Reviews Drug Discovery* **21**(9), 637–654 (2022)
- [7] Skinnider, M.A., Wang, F., Pasin, D., Greiner, R., Foster, L.J., Dalsgaard, P.W., Wishart, D.S.: A deep generative model enables automated structure elucidation of novel psychoactive substances. *Nature Machine Intelligence* **3**(11), 973–984 (2021)
- [8] Picó, Y., Barceló, D.: Pyrolysis gas chromatography-mass spectrometry in environmental analysis: Focus on organic matter and microplastics. *TrAC Trends in Analytical Chemistry* **130**, 115964 (2020)
- [9] Hollender, J., Schymanski, E., Singer, H., Ferguson, P.: Nontarget screening with high resolution mass spectrometry in the environment: Ready to go? *Environmental science & technology* (2017)
- [10] Miller, M.J., Kennedy, A.D., Eckhart, A.D., Burrage, L.C., Wulff, J.E., Miller, L.A., Milburn, M.V., Ryals, J.A., Beaudet, A.L., Sun, Q., *et al.*: Untargeted metabolomic analysis for the clinical screening of inborn errors of metabolism. *Journal of inherited metabolic disease* **38**(6), 1029–1039 (2015)
- [11] Dührkop, K., Shen, H., Meusel, M., Rousu, J., Böcker, S.: Searching molecular structure databases with tandem mass spectra using csi: Fingerid. *Proceedings of the National Academy of Sciences* **112**(41), 12580–12585 (2015)
- [12] Wei, J.N., Belanger, D., Adams, R.P., Sculley, D.: Rapid prediction of electron-ionization mass spectrometry using neural networks. *ACS central science* **5**(4), 700–708 (2019)
- [13] Goldman, S., Wohlwend, J., Stražar, M., Haroush, G., Xavier, R.J., Coley, C.W.: Annotating metabolite mass spectra with domain-inspired chemical formula transformers. *Nature Machine Intelligence* **5**(9), 965–979 (2023)
- [14] Kalia, A., Zhou Chen, Y., Krishnan, D., Hassoun, S.: Jestr: Joint embedding space technique for ranking candidate molecules for the annotation of untargeted metabolomics data. *Bioinformatics*, 354 (2025)
- [15] Stravs, M.A., Dührkop, K., Böcker, S., Zamboni, N.: Msnovelist: de novo structure generation from mass spectra. *Nature Methods* **19**(7), 865–870 (2022)

- [16] Butler, T., Frandsen, A., Lightheart, R., Bargh, B., Taylor, J., Bollerman, T., Kerby, T., West, K., Voronov, G., Moon, K., et al.: Ms2mol: A transformer model for illuminating dark chemical space from mass spectra (2023)
- [17] Bohde, M., Manjrekar, M., Wang, R., Ji, S., Coley, C.W.: Diffins: Diffusion generation of molecules conditioned on mass spectra. In: Forty-second International Conference on Machine Learning
- [18] Han, Y., Wang, P., Yu, K., Chen, L., et al.: Ms-bart: Unified modeling of mass spectra and molecules for structure elucidation. In: The Thirty-ninth Annual Conference on Neural Information Processing Systems
- [19] Rogers, D., Hahn, M.: Extended-connectivity fingerprints. *Journal of chemical information and modeling* **50**(5), 742–754 (2010)
- [20] Bajusz, D., Rácz, A., Héberger, K.: Why is tanimoto index an appropriate choice for fingerprint-based similarity calculations? *Journal of cheminformatics* **7**(1), 20 (2015)
- [21] Xie, T., Zhang, H., Yang, Q., Sun, J., Wang, Y., Long, J., Zhang, Z., Lu, H.: Csu-ms2: A contrastive learning framework for cross-modal compound identification from ms/ms spectra to molecular structures. *Analytical Chemistry* (2025)
- [22] Ruttkies, C., Schymanski, E.L., Wolf, S., Hollender, J., Neumann, S.: Metfrag relaunched: incorporating strategies beyond in silico fragmentation. *Journal of cheminformatics* **8**(1), 3 (2016)
- [23] Allen, F., Pon, A., Wilson, M., Greiner, R., Wishart, D.: Cfm-id: a web server for annotation, spectrum prediction and metabolite identification from tandem mass spectra. *Nucleic acids research* **42**(W1), 94–99 (2014)
- [24] Dührkop, K., Fleischauer, M., Ludwig, M., Aksenov, A.A., Melnik, A.V., Meusel, M., Dorrestein, P.C., Rousu, J., Böcker, S.: Sirius 4: a rapid tool for turning tandem mass spectra into metabolite structure information. *Nature methods* **16**(4), 299–302 (2019)
- [25] Bushuiev, R., Bushuiev, A., Jonge, N., Young, A., Kretschmer, F., Samusevich, R., Heirman, J., Wang, F., Zhang, L., Dührkop, K., et al.: Massspecgym: A benchmark for the discovery and identification of molecules. *Advances in Neural Information Processing Systems* **37**, 110010–110027 (2024)
- [26] Tian, Y., Krishnan, D., Isola, P.: Contrastive multiview coding. In: European Conference on Computer Vision, pp. 776–794 (2020). Springer
- [27] Zhang, Y., Ding, K., Wu, Y., Zhuang, X., Yang, Y., Zhang, Q., Chen, H.: Breaking the modality barrier: Generative modeling for accurate molecule retrieval from mass spectra. arXiv preprint arXiv:2511.06259 (2025)
- [28] Irwin, R., Dimitriadis, S., He, J., Bjerrum, E.J.: Chemformer: a pre-trained transformer for computational chemistry. *Machine Learning: Science and Technology* **3**(1), 015022 (2022)
- [29] Pudil, P., Novovicová, J., Bláha, S., Kittler, J.: Multistage pattern recognition with reject option. In: 11th IAPR International Conference on Pattern Recognition. Vol. II. Conference B: Pattern Recognition Methodology and Systems, vol. 1, pp. 92–93 (1992). IEEE Computer Society
- [30] Chow, C.-K.: An optimum character recognition system using decision functions. *IRE Transactions on Electronic Computers* (4), 247–254 (2009)
- [31] El-Yaniv, R., et al.: On the foundations of noise-free selective classification. *Journal of Machine Learning Research* **11**(5) (2010)
- [32] Geifman, Y., El-Yaniv, R.: Selective classification for deep neural networks. *Advances in neural information processing systems* **30** (2017)
- [33] Hüllermeier, E., Waegeman, W.: Aleatoric

- and epistemic uncertainty in machine learning: An introduction to concepts and methods. *Machine learning* **110**(3), 457–506 (2021)
- [34] Kendall, A., Gal, Y.: What uncertainties do we need in bayesian deep learning for computer vision? *Advances in neural information processing systems* **30** (2017)
- [35] Xu, Y.-F., Lu, W., Rabinowitz, J.D.: Avoiding misannotation of in-source fragmentation products as cellular metabolites in liquid chromatography–mass spectrometry-based metabolomics. *Analytical chemistry* **87**(4), 2273–2281 (2015)
- [36] Hendrycks, D., Gimpel, K.: A baseline for detecting misclassified and out-of-distribution examples in neural networks. In: *Proceedings of the International Conference on Learning Representations* (2017)
- [37] Bengs, V., Hüllermeier, E., Waegeman, W.: Pitfalls of epistemic uncertainty quantification through loss minimisation. *Advances in Neural Information Processing Systems* **35**, 29205–29216 (2022)
- [38] Depeweg, S., Hernandez-Lobato, J.-M., Doshi-Velez, F., Udluft, S.: Decomposition of uncertainty in bayesian deep learning for efficient and risk-sensitive learning. In: *International Conference on Machine Learning*, pp. 1184–1193 (2018). PMLR
- [39] Sale, Y., Hofman, P., Löhr, T., Wimmer, L., Nagler, T., Hüllermeier, E.: Label-wise aleatoric and epistemic uncertainty quantification. *arXiv preprint arXiv:2406.02354* (2024)
- [40] Adomavicius, G., Zhang, J.: Classification, ranking, and top-k stability of recommendation algorithms. *INFORMS Journal on Computing* **28**(1), 129–147 (2016)
- [41] Yang, J., Zhou, K., Li, Y., Liu, Z.: Generalized out-of-distribution detection: A survey. *International Journal of Computer Vision* **132**(12), 5635–5662 (2024)
- [42] Sun, Y., Ming, Y., Zhu, X., Li, Y.: Out-of-distribution detection with deep nearest neighbors. In: *International Conference on Machine Learning*, pp. 20827–20840 (2022). PMLR
- [43] Lee, K., Lee, K., Lee, H., Shin, J.: A simple unified framework for detecting out-of-distribution samples and adversarial attacks. In: *Advances in Neural Information Processing Systems*, vol. 31 (2018)
- [44] Vapnik, V.N.: An overview of statistical learning theory. *IEEE transactions on neural networks* **10**(5), 988–999 (1999)
- [45] Raymond, J.W., Willett, P.: Maximum common subgraph isomorphism algorithms for the matching of chemical structures. *Journal of computer-aided molecular design* **16**(7), 521–533 (2002)
- [46] De Waele, G., Wydmuch, M., Waegeman, W., et al.: Small molecule retrieval from tandem mass spectrometry: what are we optimizing for? *arXiv preprint arXiv:2602.16507* (2026)
- [47] Lin, T.-Y., Goyal, P., Girshick, R., He, K., Dollár, P.: Focal loss for dense object detection. In: *Proceedings of the IEEE International Conference on Computer Vision*, pp. 2980–2988 (2017)
- [48] Lakshminarayanan, B., Pritzel, A., Blundell, C.: Simple and scalable predictive uncertainty estimation using deep ensembles. *Advances in neural information processing systems* **30** (2017)
- [49] Gal, Y., Ghahramani, Z.: Dropout as a bayesian approximation: Representing model uncertainty in deep learning. In: *International Conference on Machine Learning*, pp. 1050–1059 (2016). PMLR
- [50] Daxberger, E., Kristiadi, A., Immer, A., Eschenhagen, R., Bauer, M., Hennig, P.: Laplace redux—effortless bayesian deep learning. *Advances in neural information processing systems* **34**, 20089–20103 (2021)

- [51] Hofman, P., Sale, Y., Hüllermeier, E.: Uncertainty quantification for machine learning: One size does not fit all. arXiv preprint arXiv:2512.12341 (2025)
- [52] Li, Y.L., Lu, D., Kirichenko, P., Qiu, S., Rudner, T.G., Bruss, C.B., Wilson, A.G.: Out-of-distribution detection methods answer the wrong questions. arXiv preprint arXiv:2507.01831 (2025)
- [53] Jin, Y., Candes, E.J.: Selection by prediction with conformal p-values. *Journal of Machine Learning Research* **24**(244) (2023)
- [54] Shafer, G., Vovk, V.: A tutorial on conformal prediction. *Journal of machine learning research* **9**(3) (2008)
- [55] Gascuel, O., Caraux, G.: Distribution-free performance bounds with the resubstitution error estimate. *Pattern Recognition Letters* **13**(11), 757–764 (1992)

Appendix A Uncertainty metrics

This appendix provides the formal definitions of the second-order and distance-based scoring functions summarized in Section 2.3. Throughout, we assume access to S samples $\boldsymbol{\theta}_1, \dots, \boldsymbol{\theta}_S \sim q(\boldsymbol{\theta}|\mathbf{x})$, obtained via a Bayesian approximation of $q(\boldsymbol{\theta}|\mathbf{x})$. All expectations and variances with respect to $q(\boldsymbol{\theta}|\mathbf{x})$ are approximated by their sample counterparts.

A.1 Bitwise uncertainty decomposition

Information-theoretic decomposition. Assuming independence between fingerprint bits, we model each bit probability via the marginal distribution $\theta_d \sim q_d(\theta_d|\mathbf{x})$, hence for the fingerprint bits $y_d|\theta_d \sim \text{Ber}(\theta_d)$. Let $\bar{\theta}_d = \mathbb{E}_q[\theta_d]$ denote the posterior mean for bit d . Applying the information-theoretic decomposition [38] to the mean predicted bit probability, we can derive expressions for total, aleatoric and epistemic uncertainty:

$$\underbrace{\mathbb{H}(\bar{\theta}_d)}_{u_{\text{tot}}^{(d)}} = \underbrace{\mathbb{E}_q[\mathbb{H}(y_d | \theta_d)]}_{u_{\text{al}}^{(d)}} + \underbrace{\mathbb{E}_q[D_{\text{KL}}(\theta_d || \bar{\theta}_d)]}_{u_{\text{ep}}^{(d)}}, \quad d = 1, \dots, D,$$

where $\mathbb{H}(p) = -p \log p - (1-p) \log(1-p)$ is the binary entropy. Following [39], we aggregate the bitwise uncertainties to fingerprint-level uncertainties by summing over all bits:

$$\kappa_{\text{bit}}^{(\cdot)}(\mathbf{x}) = - \sum_{d=1}^D u_{(\cdot)}^{(d)},$$

where $(\cdot) \in \{\text{tot}, \text{al}, \text{ep}\}$ and the negation ensures the convention that higher values indicate greater confidence.

A.2 Retrieval-level uncertainty decomposition

Information-theoretic decomposition. For the uncertainty on the candidate level, we look at the distribution over candidate probabilities. Each sample $\boldsymbol{\theta}_s$ induces a candidate distribution $p_j(\mathbf{x}, \boldsymbol{\theta}_s)$ via Eq. (6). Let $\bar{p}_j(\mathbf{x}) = \frac{1}{S} \sum_{s=1}^S p_j(\mathbf{x}, \boldsymbol{\theta}_s)$ denote the expected candidate probability. Following the same information-theoretic decomposition as for the fingerprint-level uncertainty, but applied to the candidate probabilities, the empirical decomposition for the retrieval-level uncertainty is given as

$$\begin{aligned} \kappa_{\text{ret}}^{\text{tot}}(\mathbf{x}) &= \sum_{j=1}^{M_i} \bar{p}_j(\mathbf{x}) \log \bar{p}_j(\mathbf{x}) \\ \kappa_{\text{ret}}^{\text{al}}(\mathbf{x}) &= \frac{1}{S} \sum_{s=1}^S \sum_{j=1}^{M_i} p_j(\mathbf{x}, \boldsymbol{\theta}_s) \log p_j(\mathbf{x}, \boldsymbol{\theta}_s), \\ \kappa_{\text{ret}}^{\text{ep}}(\mathbf{x}) &= \kappa_{\text{ret}}^{\text{tot}}(\mathbf{x}) - \kappa_{\text{ret}}^{\text{al}}(\mathbf{x}), \end{aligned}$$

where the sign convention ensures that higher values correspond to lower uncertainty. Note that $\kappa_{\text{ret}}^{\text{tot}}$ equals the negative entropy of the expected candidate distribution, while $\kappa_{\text{ret}}^{\text{al}}$ equals the negative expected conditional entropy, so that $-\kappa_{\text{ret}}^{\text{ep}}$ corresponds to the mutual information between $\boldsymbol{\theta}$ and the predicted candidate.

Rank variance. For each spectrum \mathbf{x} , let $\mathcal{S}_K(\mathbf{x})$ denote the top- K candidate set under the mean prediction $\bar{\boldsymbol{\theta}}$. For each candidate $\mathbf{c}_j \in \mathcal{S}_K(\mathbf{x})$, let $r_s(\mathbf{c}_j)$ denote its rank when candidates are re-ranked

using sample θ_s . The rank-variance scoring function is defined as

$$\kappa_{\text{rank}}(\mathbf{x}) = -\frac{1}{K} \sum_{\mathbf{c}_j \in \mathcal{S}_K(\mathbf{x})} \text{Var}_s[r_s(\mathbf{c}_j)],$$

where the variance is taken over the S posterior samples. High rank variance indicates that the relative ordering of top candidates is sensitive to parameter uncertainty, suggesting unreliable retrieval.

A.3 Distance-based scoring functions

Let $\mathbf{h}(\mathbf{x}) \in \mathbb{R}^{d_h}$ denote the penultimate-layer representation of the model for input \mathbf{x} , and let $\mathcal{H}_{\text{train}} = \{\mathbf{h}(\mathbf{x}_i)\}_{i=1}^N$ be the set of training representations.

KNN distance. Let $\mathbf{h}_1^{\text{nn}}, \dots, \mathbf{h}_k^{\text{nn}}$ be the k nearest elements of $\mathcal{H}_{\text{train}}$ to $\mathbf{h}(\mathbf{x})$ in Euclidean distance. Then

$$\kappa_{\text{knn}}(\mathbf{x}) = -\frac{1}{k} \sum_{i=1}^k \|\mathbf{h}(\mathbf{x}) - \mathbf{h}_i^{\text{nn}}\|_2.$$

Mahalanobis distance. Let $\boldsymbol{\mu} = \frac{1}{N} \sum_{i=1}^N \mathbf{h}(\mathbf{x}_i)$ and $\boldsymbol{\Sigma} = \frac{1}{N} \sum_{i=1}^N (\mathbf{h}(\mathbf{x}_i) - \boldsymbol{\mu})(\mathbf{h}(\mathbf{x}_i) - \boldsymbol{\mu})^\top$ be the sample mean and covariance of the training representations. Then

$$\kappa_{\text{mah}}(\mathbf{x}) = -\sqrt{(\mathbf{h}(\mathbf{x}) - \boldsymbol{\mu})^\top \boldsymbol{\Sigma}^{-1} (\mathbf{h}(\mathbf{x}) - \boldsymbol{\mu})}.$$

Configuration and hyperparameter search. We evaluate both scoring functions under the Deep Ensemble trained with ranking loss and with focal loss. We use the 1024-dimensional encoder representation with optional PCA dimensionality reduction to 64 or 128 components, and neighbourhood sizes $k \in \{1, 10, 50, 100\}$ for κ_{knn} . All embeddings are ℓ_2 -normalised. The best relAURC across all configurations is 0.886 (k-NN, encoder, PCA to 128 dimensions, $k=100$, Hit@20, focal loss), compared to 0.30 for confidence.

Appendix B Risk control algorithm

This appendix provides the algorithmic details of the risk control procedure described in Section 2.4, namely, the global risk control method SGR [32]. To this end, we assume access to a calibration set $\mathcal{D}_{\text{cal}} = \{(\mathbf{x}_i, \mathbf{y}_i, \mathcal{C}_i)\}_{i=1}^n$ of n i.i.d. samples from the data distribution P . In the following, let $\kappa : \mathcal{X} \rightarrow \mathbb{R}$ be a scoring function. We start by sorting the calibration samples by ascending confidence: $\kappa(\mathbf{x}_{(1)}) \leq \dots \leq \kappa(\mathbf{x}_{(n)})$. For any candidate threshold τ , one then defines the accepted subset $\mathcal{A}(\tau) = \{i : \kappa(\mathbf{x}_i) \geq \tau\}$ with $n_\tau = |\mathcal{A}(\tau)|$, and the empirical selective risk on this subset:

$$\hat{r}(\tau) = \frac{\sum_{i \in \mathcal{A}(\tau)} \ell_K(\mathbf{x}_i, \mathbf{y}_i)}{n_\tau}.$$

Since $\ell_K \in \{0, 1\}$, the number of errors $k_\tau = \sum_{i \in \mathcal{A}(\tau)} \ell_K(\mathbf{x}_i, \mathbf{y}_i)$ among n_τ accepted samples is a sufficient statistic. The Clopper–Pearson upper bound [55] $B^*(\hat{r}, \delta', n_\tau)$ is the solution b of

$$\sum_{j=0}^{k_\tau} \binom{n_\tau}{j} b^j (1-b)^{n_\tau-j} = \delta',$$

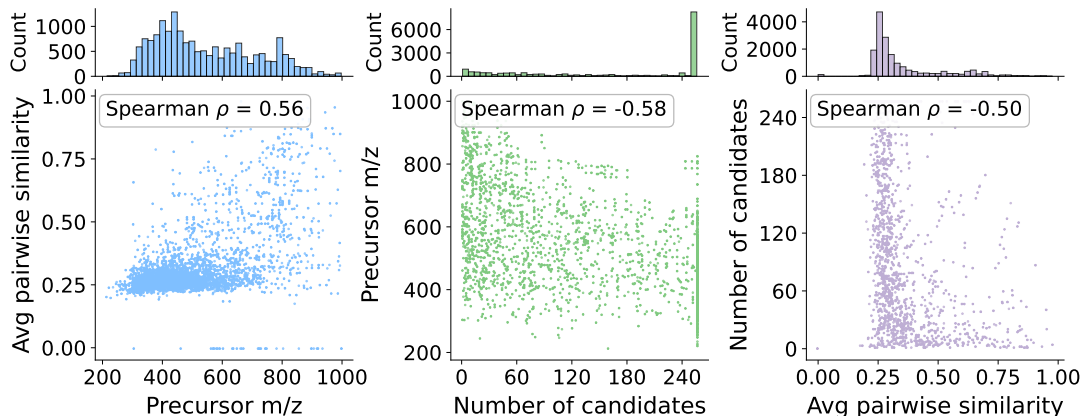


Fig. C1: Pairwise scatter plots of precursor mass, average pairwise cosine similarity and number of candidates per spectrum in the candidate sets of the MassSpecGym test set. Spearman rank correlations are shown in each panel. Histograms on the top and right axes show the marginal distribution of each variable. Larger candidate sets arise for lower precursor masses and contain more structurally diverse candidates.

which yields the tightest b such that $\mathbb{P}(R(f, g_\tau) > b) < \delta'$ for a fixed threshold τ . The SGR algorithm performs a binary search over threshold indices $z \in \{1, \dots, n\}$, examining at most $k = \lceil \log_2 n \rceil$ thresholds. At iteration i , it sets $\tau = \kappa(\mathbf{x}_{(z)})$, computes the empirical risk $\hat{r}(\tau)$, and evaluates the bound $b_i^* = B^*(\hat{r}, \delta/k, n_\tau)$ with adjusted significance δ/k . If $b_i^* < r^*$, the search moves toward higher coverage (lower z), otherwise toward lower coverage (higher z). The output is the final threshold τ^* and bound b^* , satisfying the guarantee

$$\mathbb{P}(R(f, g_{\tau^*}) > b^*) < \delta.$$

Appendix C Experimental details

C.1 Dataset characterisation

The MassSpecGym test set contains 17 556 spectra with candidate set sizes ranging from 1 to the benchmark cap of 256. Figure C1 characterises the candidate sets obtained by filtering by molecular formula through three pairwise relationships. Candidate set size correlates negatively with precursor mass: heavier molecules have fewer database matches, yielding smaller candidate sets. At the same time, larger candidate sets exhibit lower average pairwise cosine similarity among their members, indicating greater structural diversity. These two effects are linked: low-mass molecules are more densely represented in chemical databases, producing large candidate sets of structurally diverse molecules, while high-mass molecules yield small, structurally homogeneous candidate sets. This variation has direct consequences for both retrieval difficulty and uncertainty estimation, as analyzed in Section 3.3.

C.2 Model architecture and training

The base model is a three-layer MLP following the fingerprint predictor of De Waele et al. [46] The input spectrum is binned with binwidth 0.1 Da, yielding a vector $\mathbf{x} \in \mathbb{R}^{10050}$. Three fully connected layers with hidden dimension 1024, GeLU activations, layer normalisation and dropout ($p = 0.3$) map the input to a 1024-dimensional representation. A linear output layer $W_{\text{out}} \in \mathbb{R}^{4096 \times 1024}$ followed by a component-wise sigmoid produces the fingerprint prediction $\boldsymbol{\theta} = \sigma(W_{\text{out}} f(\mathbf{x})) \in [0, 1]^{4096}$. We train two model variants. The first is trained with focal loss [47] on individual bits ($\gamma = 2.0$, learning rate 3×10^{-4}). The second is trained with the contrastive ranking loss (Eqn. 10) using cosine similarity and temperature $T = 0.003$

(learning rate 1×10^{-4}). Both variants use the Adam optimizer, a batch size of 64, gradient clipping at 1.0 and are trained for a maximum of 50 epochs. Model selection is based on the best validation Hit@20 under cosine similarity retrieval.

C.3 Posterior approximation methods

Deep Ensemble. Five copies of the base model are trained independently with different random initialisations (seeds 42–46) and data-loader shuffles. Model selection is performed per member independently.

MC Dropout. A single trained model (one ensemble member) is evaluated with dropout enabled at test time, using $S = 50$ stochastic forward passes with the training dropout rate ($p = 0.3$).

Laplace approximation. A diagonal last-layer Laplace approximation [50] is fitted to a single trained model. The posterior is a Gaussian over the final linear layer W_{out} , with precision estimated via the diagonal generalised Gauss–Newton (GGN) approximation accumulated over 200 training batches. The prior precision is tuned via marginal likelihood maximisation over a logarithmically spaced grid. At test time, $S = 50$ weight samples are drawn and passed through the sigmoid to produce fingerprint probability samples.

Appendix D Further experimental results

D.1 Fingerprint similarity loss rejection

The main analysis in Section 3.2 evaluates selective prediction with the retrieval loss $\ell_K = 1 - \text{Hit}@K$, where retrieval-level scoring functions such as confidence and aleatoric uncertainty achieve the best risk-coverage tradeoffs. Here we evaluate with fingerprint-level similarity losses to test whether the level-alignment principle extends bidirectionally.

Similarity losses. Let $\bar{\boldsymbol{\theta}} \in [0, 1]^D$ denote the ensemble-mean predicted probabilities and $\hat{\mathbf{y}} = \mathbb{I}[\bar{\boldsymbol{\theta}} > 0.5] \in \{0, 1\}^D$ the binarised prediction, with ground truth $\mathbf{y} \in \{0, 1\}^D$. We consider three similarity measures, each of which can be evaluated with either the continuous or the discrete predicted fingerprint:

$$\begin{aligned} \text{Tanimoto}(\mathbf{a}, \mathbf{y}) &= \frac{\sum_j a_j y_j}{\sum_j a_j + \sum_j y_j - \sum_j a_j y_j}, \\ \text{Cosine}(\mathbf{a}, \mathbf{y}) &= \frac{\mathbf{a}^\top \mathbf{y}}{\|\mathbf{a}\|_2 \|\mathbf{y}\|_2}, \\ \text{Hamming}(\mathbf{a}, \mathbf{y}) &= 1 - \frac{1}{D} \sum_{j=1}^D \mathbb{I}[a_j \neq y_j], \end{aligned}$$

where $\mathbf{a} = \bar{\boldsymbol{\theta}}$ for the continuous prediction and $\mathbf{a} = \hat{\mathbf{y}}$ for the discrete prediction. The corresponding losses are $\ell_{\text{sim}} = 1 - \text{sim}(\mathbf{a}, \mathbf{y})$. Hamming loss requires binary inputs and is therefore always evaluated on $\hat{\mathbf{y}}$.

Continuous evaluation. When Tanimoto and cosine similarity are evaluated on the continuous probabilities, the loss is sensitive not only to which bits cross the binarisation threshold, but also to how far each prediction is from it. Table D1 (left) shows that bitwise total uncertainty achieves the lowest relAURC for both Tanimoto and cosine loss, reversing the retrieval-level dominance observed for hit rate. This pattern is consistent across all three posterior approximation methods. The explanation is that continuous Tanimoto and bitwise total uncertainty measure the same property: both are determined by how peaked the per-bit probabilities are near zero or one, rather than by which side of the decision boundary they fall on.

Table D1: Selective prediction quality for fingerprint-level similarity losses, reported as relAURC (Eqn. 9). Lower is better. Left: continuous evaluation on predicted probabilities $\hat{\theta}$. Right: discrete evaluation on binarised fingerprints $\hat{y} = \mathbb{I}[\hat{\theta} > 0.5]$. Hamming always uses discrete inputs. Results are shown for the Deep Ensemble ($S = 5$) trained with focal loss, and the experimental setup as described in Section 2.6.

κ	Continuous		Discrete		Ham.
	Tan.	Cos.	Tan.	Cos.	
<i>Fingerprint-level</i>					
$\kappa_{\text{bit}}^{\text{tot}}$ total	0.367	0.712	0.818	0.974	1.335
$\kappa_{\text{bit}}^{\text{al}}$ aleatoric	0.534	0.713	0.853	0.971	1.171
$\kappa_{\text{bit}}^{\text{ep}}$ epistemic	1.142	1.150	1.099	1.061	0.777
<i>Retrieval-level</i>					
$\kappa_{\text{ret}}^{\text{al}}$ aleatoric	0.755	0.768	0.809	0.867	1.156
κ_{conf} confidence	0.826	0.835	0.859	0.908	1.130
κ_{rank} $K=5$	0.852	0.871	0.849	0.900	1.062
<i>Other</i>					
$ \mathcal{C} $ num. candidates	0.921	0.948	1.002	1.033	1.255

Discrete evaluation. To test whether this alignment reflects genuine substructure-level prediction quality or merely probability calibration, we repeat the analysis with the binarised fingerprint (Table D1, right). The advantage of bitwise scoring functions largely vanishes: bitwise entropy, which is entirely about distance-from-boundary, loses its predictive power. This reveals that the apparent level alignment in the continuous setting was driven by a coupling between bitwise entropy and probability calibration, rather than by genuine predictive value at the substructure level.

Hamming loss. Nearly all scoring functions perform worse than random rejection ($\text{relAURC} > 1$), because Hamming weights all bits equally while both bitwise and retrieval-level scoring functions concentrate their signal on the sparse minority of active bits. The sole exception is bitwise epistemic uncertainty, which captures disagreement on inactive bits that other scores ignore: on these bits the aleatoric component vanishes, so any inter-sample disagreement manifests entirely as epistemic uncertainty. This gives it a more uniform sensitivity across all bits, matching the uniform weighting of Hamming loss.

D.2 Scoring function correlations

Figure D2 shows the pairwise Spearman rank correlations between all scoring functions for the Deep Ensemble trained with focal loss (top) and ranking loss (bottom). The overall structure is consistent across both training objectives, with two features standing out. First, the retrieval-level and fingerprint-level scoring functions form nearly independent blocks: correlations across the two groups are close to zero. This confirms that the two levels capture fundamentally different aspects of prediction quality, consistent with the finding in Section 3.2 that fingerprint-level scores are poor proxies for retrieval-level task losses. Second, within the retrieval-level block, confidence, aleatoric uncertainty, total uncertainty, and the number of candidates are strongly correlated. This clustering is particularly tight under ranking loss, where the retrieval scoring function is explicitly optimized. Rank variance interpolates between this cluster and the remaining scores as K increases: at $K=20$ it aligns closely with confidence and aleatoric uncertainty, while at $K=1$ it is more weakly coupled. Score gap and retrieval epistemic uncertainty are both largely decoupled from the other retrieval-level scores, explaining their distinct behavior in the risk-coverage analysis.

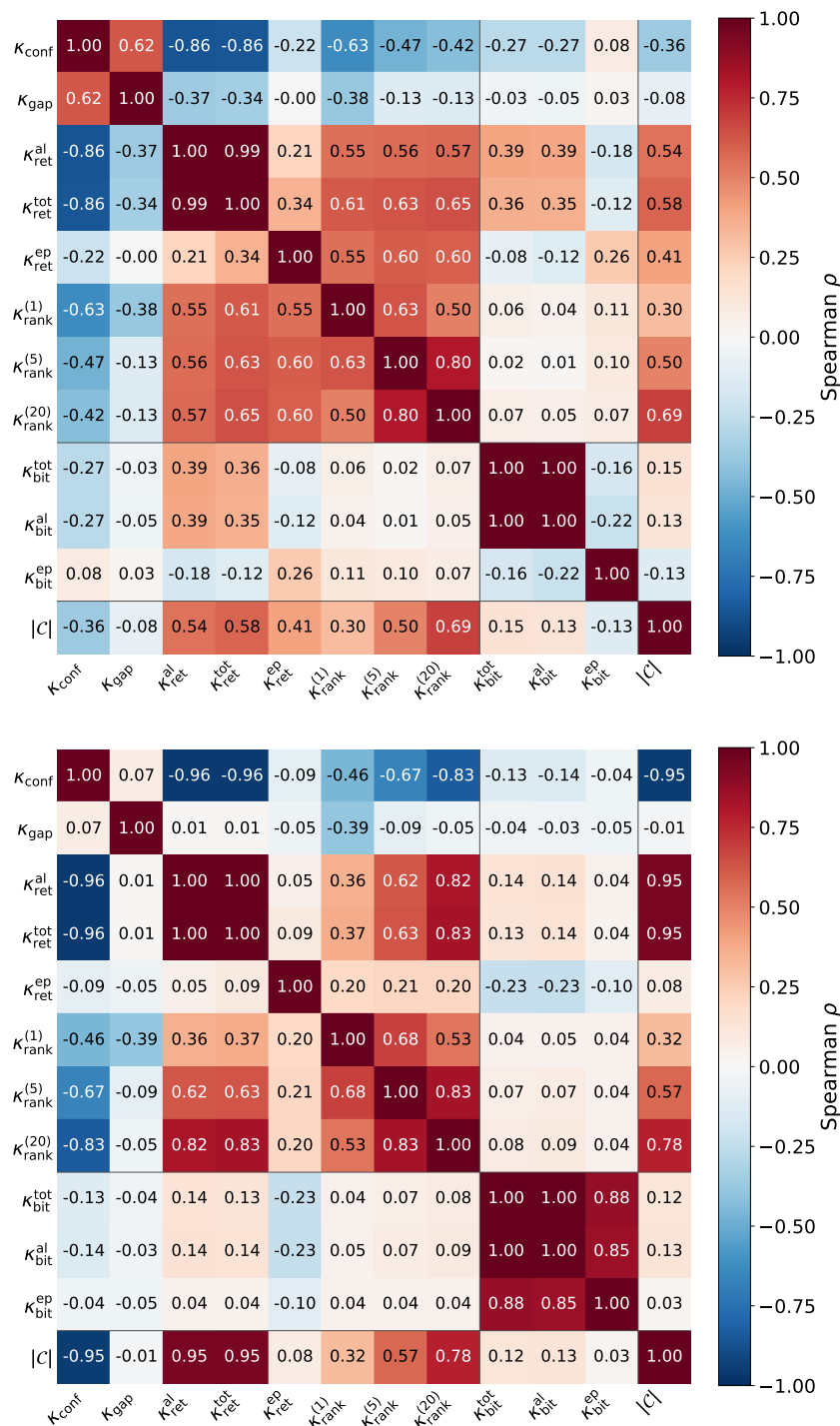


Fig. D2: Pairwise Spearman rank correlations between scoring functions for the Deep Ensemble on the MassSpecGym test set. Top: focal loss with fingerprint aggregation. Bottom: ranking loss with score aggregation. Horizontal and vertical lines separate retrieval-level, fingerprint-level, and external scoring functions.